INORGANIC CHEMISTRY

FRONTIERS

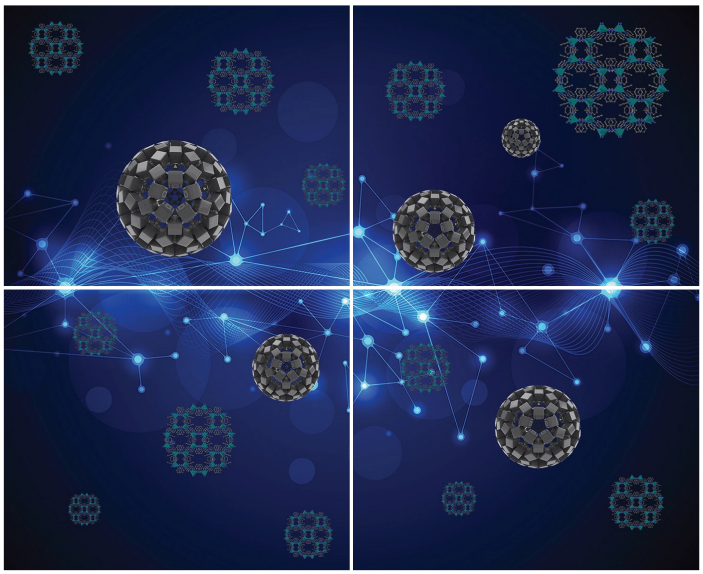

Accepted Manuscript

This article can be cited before page numbers have been issued, to do this please use: B. T. W. Lo, J. Ling, J. Miao, Z. Tao, C. Lin and H. Wang, *Inorg. Chem. Front.*, 2026, DOI: 10.1039/D6QI00842A.

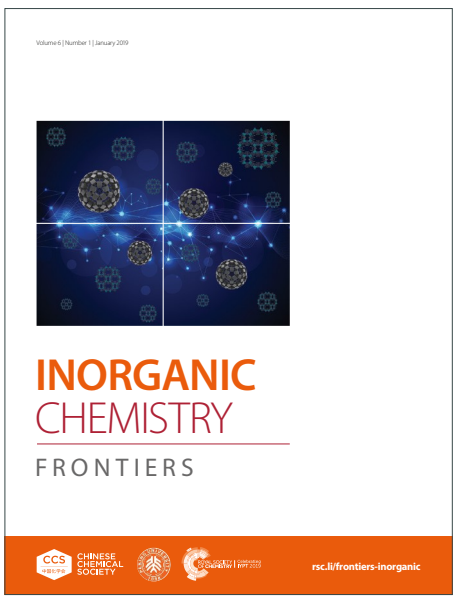

View Article Online
DOI: 10.1039/D6QI00842A

ARTICLE

Countercation-Regulated Pore Structure Engineering of fcu-Metal-Organic Frameworks for Enhanced Gas Separation

Received 00th January 20xx,
Accepted 00th January 20xx

DOI: 10.1039/x0xx00000x

Jing Ling[a,b], Zhiyu Tao[a], Jiafeng Miao[b], Cong Lin[a,c*], Hao Wang[b*], Tsz Woon Benedict Lo[a,c,d*]

Metal–organic frameworks (MOFs) offer exceptional structural tunability for targeted gas adsorption and separation; however, traditional pore engineering via organic ligand functionalisation often necessitates complex synthetic routes. In contrast, substituting inorganic secondary building units (SBUs) offers a streamlined strategy for modulating the pore environment, particularly when introducing metals with varied valences that require charge-balancing counterions. Herein, we elucidate the regulatory role of extra-framework cations by conducting a comparative study between the anionic yttrium-based framework (Y-fum-fcu-MOF) and its neutral zirconium analogue (Zr-fum-fcu-MOF, MOF-801). Through high-resolution synchrotron X-ray powder diffraction and Rietveld refinement, we identify a unique 'pincer-like' coordination mechanism within the Y-MOF cavities, where CO_2 molecules are synergistically stabilised by Y^{3+} centres and protonated dimethylammonium ($DMA\text{-}H^+$) counteraction. This cooperative interaction effectively constrains the rotational and translational degrees of freedom of the guest molecules, resulting in a significantly enhanced isosteric heat of adsorption (Q_{st} = 38 kJ mol^{-1}). Consequently, Y-MOF exhibits a CO_2 uptake of 85.11 $cm^3\ g^{-1}$ at 273 K, representing a 46.4% increase over the neutral Zr-MOF, alongside superior CO_2/N_2 selectivity. These findings demonstrate that counteraction engineering can induce localised 'electrostatic locking' of guest molecules, providing a robust molecular-level blueprint for designing high-performance adsorbents for industrial carbon capture and gas separation.

Introduction

The efficient capture and separation of CO_2 represent a critical challenge in mitigating climate change and enabling the transition toward sustainable energy systems[1]. Among the wide range of porous materials investigated for gas separations, metal–organic frameworks (MOFs) have emerged as the leading candidates due to their high structural tunability, large specific surface areas, and versatile chemical functionalities[2]. These hybrid organic–inorganic solids provide a versatile platform for tailoring pore properties and surface chemistry, thereby enabling the selective sequestration of CO_2 over competing species such as N_2[3].

Efforts to optimise gas adsorption performance of MOFs have largely relied on the functionalisation of organic ligands[4]. However, pore regulation based solely on linker engineering often faces significant challenges in organic synthesis[5]. In this context, pore engineering of MOFs by modulating inorganic building units offers a viable alternative. The isoreticular substitution of secondary building units (SBUs), where nodes composed of different metals but with similar connectivity are exchanged while preserving the overall structural topology, has played a crucial role in fine-tuning the pore geometry and dimensions of MOFs[6]. For example, replacing tetravalent Zr_6 clusters with trivalent Y_6 ones in topologies such as fcu, ftw, or soc provides a robust strategy to transition from a neutral framework to an anionic one[7]. This SBU engineering approach is particularly significant as it induces a charge imbalance that necessitates the incorporation of extra-framework countercations. These cations, in turn, act as intra-pore segmenting agents that significantly enhance the localized electric field and pore polarity, which are critical for discriminating between gases with different polarizabilities or quadrupole moments, such as CO_2 and N_2. In our previous study, we demonstrated that the substitution of Zr_6 clusters with Y_6 ones in ftw-type MOFs generates pore environments that are optimal for the precise separation of propane and propylene[6]. Nevertheless, the influence of these charge-balancing counterions on pore structure regulation remains poorly understood.

In this work, we address this underexplored matter by investigating the impact of charge-balancing counteraction within an anionic MOF on CO_2 adsorption. We employ a unique comparative model incorporating two topologically identical but electronically distinct frameworks: a negatively charged yttrium-based Y-fum-fcu-MOF ('Y-MOF') and its charge-neutral zirconium-based analogue, Zr-fum-fcu-MOF ('Zr-MOF'). Both materials exhibit the fcu topology, constructed from hexanuclear clusters, $[Y_6(OH)_8(COO)_{12}]^{2-}$ for Y-MOF and $[Zr_6O_4(OH)_4(COO)_{12}]$ for Zr-MOF, which are interconnected by fumarate ligands ($^-OOC–CH=CH–COO^-$)[8,9].

[a] Department of Applied Biology and Chemical Technology, The Hong Kong Polytechnic University, Hung Hom, Hong Kong, China
[b] Hoffmann Institute of Advanced Materials, Shenzhen Polytechnic University, Shenzhen, China.
[c] PolyU-Daya Bay Technology and Innovation Research Institute, The Hong Kong Polytechnic University, Huizhou, Guangdong, China
[d] Department of Applied Physics, The Hong Kong Polytechnic University, Hung Hom, Hong Kong, China.

Compared to the inherently neutral Zr-MOF framework, replacing tetravalent Zr^{4+} with trivalent Y^{3+} yields a negatively charged framework in Y-MOF. Therefore, counteractions, the protonated dimethylammonium (DMA-H^+) derived from the decomposition of the synthetic solvent N,N-dimethylformamide (DMF), are necessarily introduced outside the framework to maintain charge neutrality[10]. The application of Rietveld refinement to synchrotron X-ray powder diffraction (PXRD) data has enabled the clear elucidation of the adsorption structures of CO_2 and identification of key structural responses within the two host frameworks. Besides, various characterisation methods were carried out to elucidate the mechanistic influence of these cations in Y-MOF on gas uptake and selectivity. Our findings provide a fundamental blueprint for counterion engineering in pore regulation for enhanced regulation of gas adsorption/separation.

Results and discussion

With specific acid regulators (formic acid and 2-fluorobenzoic acid), Y^{3+} and Zr^{4+} metal sources were combined with fumaric acid (HOOC–CH=CH–COOH) ligand to construct respective anionic Y-MOF and neutral Zr-MOF via a solvothermal method[8,9]. To satisfy the substantial sample requirements for comprehensive gas adsorption measurements and dynamic breakthrough experiments, the synthesis of Y-MOF was effectively scaled up 10-fold. This not only ensured sufficient samples for multi-dimensional characterisations but also demonstrated the robustness and scalability of the synthetic protocol, yielding products with consistent crystallinity and porosity. And prior to gas adsorption and separation, we carefully performed solvent exchange (with ethanol) and subsequent heat treatment. These steps target to remove most physisorbed DMF species from synthesis[11].

To evaluate the structural robustness of the obtained Y-MOF and Zr-MOF throughout the processing stages, we conducted a series of PXRD measurements to track along the synthesis steps (**Figure S1** in the Supporting Information (SI) for the as-synthesised, ethanol-exchanged, and activated samples). The PXRD profiles of the as-synthesised Y-MOF and Zr-MOF both exhibit sharp, strong reflections that perfectly match their respective simulated patterns, confirming the high crystallinity. Following ethanol-exchange for seven days, sharp Bragg diffraction peaks maintain, demonstrating the framework's stability to withstand solvothermal stress and internal capillary forces. Crucially, the activated samples, obtained after outgassing at 150 °C under high vacuum, retain their crystalline integrity without any observable peak broadening or phase transition. This consistency underscores the permanent porosity and exceptional thermal stability of both the anionic and neutral fcu frameworks, ensuring a reliable structural platform for subsequent gas adsorption and separation cycles. Additionally, the Fourier transform infrared (FTIR) spectra show the characteristic vibrational bands of Y-MOF (**Figure S2**), further confirming its structural robustness, whereas presence of residual DMF is evidenced by solid-state nuclear magnetic resonance (NMR) (**Figure S3**). Besides, elemental analysis (**Table S1**) shows good agreement with the proposed molecular compositions of both MOFs, indicating the absence of significant bulk impurities.

The high-resolution synchrotron PXRD data along with refinement of the activated Y-MOF and Zr-MOF are presented in **Figure 1a** and **1b**. All observed reflections are consistent with the calculated Bragg positions for the cubic $Pn\bar{3}$ lattice, indicating the absence of symmetry lowering or phase transformation. Highly symmetric Bragg peaks also indicate the homogeneity of the Y-MOF and Zr-MOF, which possess comparable lattice parameters of 17.9079 Å and 18.5813 Å and unit cell volumes of 5743.01 $Å^3$ and 6415.55 $Å^3$, respectively.

We subsequently investigated the Fourier difference maps with the framework atoms constrained to visualise the occupancy and spatial distribution of the extra-framework species within the two MOFs. Apparent residual electron density features could be indicative of the proposed crystallographic locations of the DMA-H^+ cations. Significant electron density was observed in Y-MOF (**Figure 1c**) near the carboxylate oxygen atoms of the fumarate linkers, suggesting strong electrostatic interactions between the extra-framework cations and the anionic framework. In contrast, we observed minimal electron density in the extra-framework space of Zr-MOF (**Figure S4**).

Given the high crystallinity of the Y-MOF and Zr-MOF samples, Rietveld refinement of the synchrotron PXRD data was conducted to determine the atomic positions based upon above Fourier map analysis. Structural models were obtained via simulated annealing, which can identify energetically favourable positions of the guest species within the pore environment[12,13]. Although both Y-MOF and Zr-MOF adopt the fcu topology featuring octahedral and tetrahedral cavities, they exhibit different cavity occupancies (**Figure 1d** and **1e**). While the cavities of the neutral Zr-MOF remain vacant, the cubic cages of Y-MOF are populated by DMA-H^+ cations. The Rietveld-derived crystal structure of Y-MOF identifies a critical N_{DMA}(–H)···$O_{Y\text{-}MOF}$ distance of 3.33 Å between the nitrogen atom of the DMA-H^+ cations and the μ_3-O atom of the $Y_6(OH)_8$ cluster[14]. This distance is indicative of hydrogen-bonding along the H atom of DMA and framework O atom, which shows that the DMA-H^+ species are not merely transient guests but are stably localised within the framework channels electrostatically. The zoom-in figure further highlights the specific host–guest interactions of DMA-H^+ cations in Y-MOF.

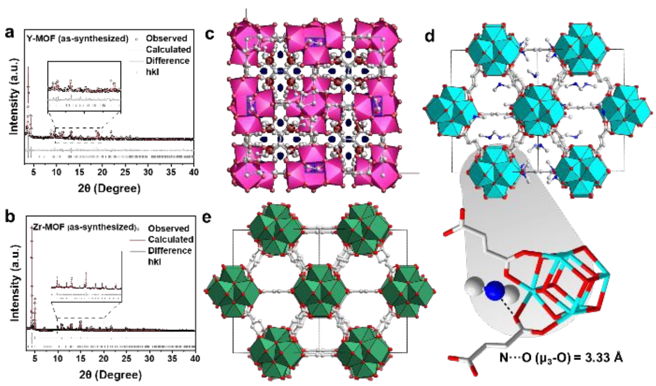

Figure 1. Rietveld refinement profiles of synchrotron PXRD data collected at 298 K (E = 20 keV, λ = 0.6199 Å) for (**a**) Y-MOF and (**b**) Zr-MOF. Detailed atomic parameters and crystallographic data are provided in **Table S2–S5**. (**c**) Fourier difference map of Y-MOF. The crystal structures of (**d**) Y-MOF and (**e**) Zr-MOF derived from Rietveld refinement. Specific host-guest interactions of DMA-H^+ cations in Y-MOF are shown in the zoom-in figure. Ball-and-stick representation: light blue, Y; green, Zr; red, O; dark blue, N; grey, C. Hydrogen atoms are omitted for clarity.

View Article Online DOI: 10.1039/D6QI00842A

To evaluate and compare the permanent porosity of Y-MOF and Zr-MOF, N_2 adsorption-desorption measurements were conducted at 77 K (**Figure 2a**). The pore size distribution of Y-MOF and Zr-MOF were subsequently calculated (**Figure S5**). Both materials exhibit typical type I adsorption profiles, characteristic of microporous architectures. A slight hysteresis observed in the adsorption isotherm of Zr-MOF may be attributed to the presence of structural defects, consistent with previous reports[15]. The apparent Brunauer-Emmett-Teller (BET) specific surface areas and total pore volumes were calculated to be 821.9 $m^2 g^{-1}$ and 0.833 $cm^3 g^{-1}$ for Zr-MOF, and 707.4 $m^2 g^{-1}$ and 0.190 $cm^3 g^{-1}$ for Y-MOF, respectively. Compared to Zr-MOF, Y-MOF exhibits a slightly lower specific surface area and total pore volume. A reduction in the effective pore diameter from ~9.1 Å in Zr-MOF to ~4.1 Å in Y-MOF, as estimated from BET analysis, was observed. This pore diameter reduction can be attributed to the presence of DMA-H^+ cations, which occupy a significant portion of the void space within the anionic Y-based framework to maintain overall charge neutrality[16]. This steric occupation, together with the positive charge of the DMA-H^+ species, can alter the polarity within the internal pore environment of Y-MOF[17].

The existence of the DMA-H^+ cations in Y-MOF is supported by our temperature-programmed desorption mass spectrometry (TPD–MS) results (**Figure 2b**). In the temperature range between 130 and 230 °C, a peak centred at 195 °C appeared. This indicates desorption of the DMF molecules (73 m/z) in large quantities, which are physically or weakly chemically adsorbed onto the MOF surface. As the temperature further increased to 230–320 °C, the TPD–MS profile exhibited a remarkable change. Specifically, at around 270 °C, the DMF signal significantly weakened, while the signals from DMA (45 m/z) and CO (28 m/z) surged dramatically, forming a sharp, highly overlapping peak. This shows that DMF molecules remaining at the strongly adsorbed sites overcome the reaction energy barrier at this temperature, undergoing decarboxylation and breaking down into the DMA and CO.

Thermogravimetric analysis (TGA) was conducted to investigate the thermal stability of the Y-MOF and Zr-MOF, as shown in **Figure 2c** and **2d**. For Y-MOF, the TGA profile reveals a distinct three-stage mass loss. The initial weight loss of 12.1% up to 200 °C is attributed to the removal of guest water/ethanol molecules. A subsequent mass loss of 8.41% (from 87.90% to 79.49%) occurs between 200 and 350 °C, corresponding to the decomposition and release of framework-embedded DMA-H^+ cations. A distinct weight loss plateau is observed until 595 °C, where a sharp 25.17% mass loss indicates the final decomposition of the organic framework. In comparison, Zr-MOF exhibits an initial mass loss of 9.58% below 100 °C corresponds to the removal of physiosorbed water and ethanol. A secondary loss of 25.67% (from 90.42% to 64.75%) up to 350 °C is attributed to residual DMF and possible coordinated terminal solvents at the missing-linker sites, with the framework collapse occurring at a slightly lower temperature of 550 °C. These results demonstrate that the Y-based framework not only possesses higher thermal stability but also highlights the cleaner activation profile achieved via the ethanol-exchange process. **Figure S6** shows the TGA profiles of Y-MOF and Zr-MOF in air. When the temperature reaches 600 °C, the Y-MOF is completely converted to Y_2O_3, and the Zr-MOF is completely converted to ZrO_2. Our temperature-programmed synchrotron PXRD dataset also reveals that both Y-MOF and Zr-MOF exhibit excellent thermal stability (**Figure S7**).

The morphological features of the as-synthesised Y-MOF and Zr-MOF were evaluated using scanning electron microscopy (SEM). As illustrated in **Figure 2e** and **2f**, both MOFs possess well-defined polyhedral particles with smooth facets and uniform particle size distributions. Notably, the particle size distribution of Y-MOF shows an average particle size of 19 µm, which is significantly larger than that of Zr-MOF (0.833 nm). The increased particle size of Y-MOF may be attributed to the extra-framework counteractions, which could promote the growth and assembly of the MOF framework[18].

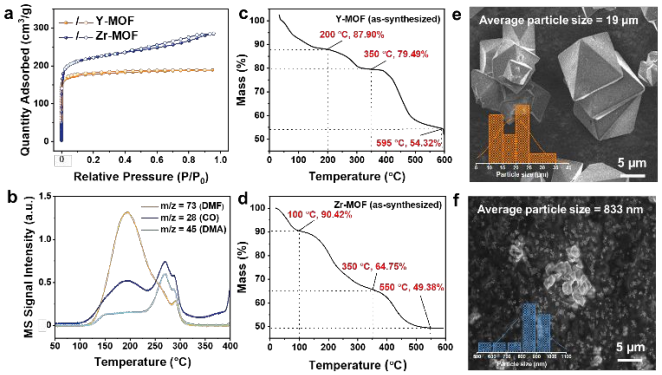

Figure 2. (**a**) Adsorption−desorption isotherm of N_2 at 77 K for Y-MOF and Zr-MOF. (**b**) TPD-MS profiles of the activated Y-MOF, verifying the thermal decomposition of DMF (m/z = 73) into DMA (m/z = 45) and CO (m/z = 28). TGA in N_2 profiles of (**c**) Y-MOF and (**d**) Zr-MOF. SEM images and particle size distribution of (**e**) Y-MOF and (**f**) Zr-MOF.

The CO_2 capture performance of Y-MOF and Zr-MOF is subsequently investigated, given that they have markedly different pore environment but similar pore architectures. The CO_2 and N_2 adsorption isotherms at 273, 288, and 298 K are shown in **Figure 3a** and **3b**, demonstrating type I adsorption profiles for both MOFs, indicative of their microporous nature. Notably, despite lower specific surface area, Y-MOF consistently demonstrates a higher CO_2 uptake than Zr-MOF across the entire temperature and pressure range.

Specifically, at 273 K and 1 bar, Y-MOF achieves a CO_2 capacity of 85.11 $cm^3 g^{-1}$, corresponding to an increasement of 46.4% compared to the 58.12 $cm^3 g^{-1}$ observed for Zr-MOF (**Figure S8**). Building on Y-MOF's superior uptake capacity, a thermodynamic analysis of the isosteric heat of adsorption (Q_{st}) calculated using the Clausius-Clapeyron equation (**Equation 1**) was conducted to elucidate the underlying energetic contributions to this enhancement. Based on the CO_2 adsorption isotherms at 273, 288, and 298 K, the Q_{st} values of Y-MOF was determined ranging between 32 and 38 kJ mol^{-1}, notably higher than the 24 and 28 kJ mol^{-1} observed for Zr-MOF. This enhanced adsorption enthalpy is driven by the dipole-quadrupole interactions arising from the localized positive charge of DMA-H^+ cations. Unlike the passive pores in Zr-MOF where CO_2 resides in a disordered state, the cation-decorated pores in Y-MOF generate a

higher electrostatic potential gradient[19]. This gradient may affect the polarization of the CO_2 molecules, which is attributable to the 35.7% elevation in Q_{st} (from 28 to 38 kJ mol^{-1}).

$$lnP = \frac{-Q_{st}}{RT} + lnC \qquad \textbf{Equation (1)}$$

where P is the pressure, Q_{st} is the isosteric heat of adsorption, R is the ideal gas constant (8.314 J/mol·K), T is the temperature, and C is a constant.

Besides, the separation performance for CO_2/N_2 mixtures was initially evaluated using the ideal adsorbed solution theory (IAST) for an equimolar mixture at 298 K. And the results show that Y-MOF demonstrates a selectivity of 10.59, exceeding the value of 9.46 obtained for Zr-MOF. The detailed computational procedures are provided in the Supporting Information.

$$Selectivity = \frac{q_{CO2}/q_{N2}}{y_{CO2}/y_{N2}} \qquad \textbf{Equation (2)}$$

where q_{CO2} and q_{N2} represents the adsorption amounts of CO_2 and N_2 under equilibrium conditions (mmol g^{-1}), y_{CO2} and y_{N2} are the corresponding mole fractions in the gas phase for the mixtures.

This preferential adsorption behaviour could be associated with the higher electropositivity and ionic character of the trivalent Y^{3+} nodes, which, in conjunction with the DMA-H^+ cations, generate a more polarised pore environment that favours interactions with CO_2 over N_2[20]. The enhanced thermodynamic affinity arising from these specific cation–guest interactions directly correlate with the MOF's improved ability to discriminate between gas species[21]. However, as static selectivity models may not fully substantiate the complexities of practical operation, dynamic breakthrough experiments are necessary to validate the separation performance under realistic flow conditions[22].

Dynamic breakthrough experiments were then conducted using a 50:50 (v/v) CO_2/N_2 mixture at 298 K (**Figure 3c** and **3d**). For both Y-MOF and Zr-MOF, N_2 elutes almost immediately, whereas CO_2 is preferentially retained within the frameworks. Notably, Y-MOF exhibits a substantially prolonged CO_2 breakthrough time, confirming its stronger thermodynamic affinity and enhanced dynamic selectivity to CO_2. However, a kinetic trade-off is observed: while Y-MOF provides stronger host–guest interactions, the larger and unoccupied pore structure of Zr-MOF facilitates more rapid gas diffusion[23,24].

Consistent with the higher CO_2 uptake observed in the static isotherms (**Figure 3a**), Y-MOF exhibits a significantly prolonged breakthrough time for CO_2 compared to Zr-MOF (**Figure 3c and 3d**). This extended retention time, coupled with a broader breakthrough profile, confirms that Y-MOF possesses a substantially higher total dynamic adsorption capacity even under continuous flow regimes. The presence of extra-framework DMA-H^+ cations within the Y-MOF pores provides superior thermodynamic selectivity and enhanced binding affinity, effectively capturing CO_2 molecules more efficiently than the neutral Zr-MOF. Despite the narrower pore aperture (4.1 Å), the synergistic interactions between the Y^{3+} centers and the cations do not impede the overall capture efficiency; instead, they transform the pore space from a passive void into a highly chemically active environment that facilitates superior gas discrimination. Consequently, Y-MOF demonstrates excellent potential for practical carbon capture applications, outperforming its zirconium analogue in both thermodynamic capacity and dynamic separation performance. This modification establishes a direct correlation between framework charge, pore polarity, and CO_2 capture performance[25,26].

The strength of these interactions was further investigated using TPD–MS (**Figure 3e** and **3f**). Specifically, Y-MOF exhibits a CO_2 desorption peak at a significantly higher temperature (~300 °C) along with greater intensity than that of Zr-MOF (~270 °C), highlighting the increased thermodynamic affinity of CO_2 for the counteraction-regulated framework. This behaviour indicates the pore environment of Y-MOF enables more effective sequestration of CO_2 and requires higher energy for desorption[18].

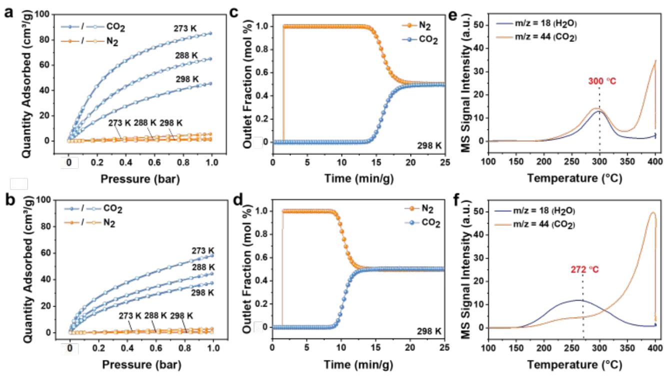

Figure 3. CO_2 and N_2 adsorption-desorption isotherms for (**a**) Y-MOF and (**b**) Zr-MOF measured at 273, 288, and 298 K (detailed isotherms are also presented in **Figure S7**). Filled and open symbols represent adsorption and desorption branches, respectively. Experimental breakthrough curves for an equimolar CO_2/N_2 mixture (50:50 v/v) at 298 K and 1 bar for (**c**) Y-MOF and (**d**) Zr-MOF. TPD-MS profiles for (**e**) Y-MOF and (**f**) Zr-MOF after CO_2 adsorption.

By taking advantage of the molecular specificity of the adsorbate species, with the significant alteration in scattering parameters of the underneath adsorbent atoms, their host-guest interactions with the MOF framework (and also in zeolites) at an atomistic level can be elucidated[27,28]. The high brilliance and angular resolution of modern synchrotron X-ray facilities enable precise localisation of CO_2 molecules within the framework, as shown by high signal-to-noise ratios (near-zero intensity between peaks) and the clear separation between closely spaced peaks[29]. Upon loading with CO_2, we observed pronounced changes in the intensities of the Bragg reflections (**Figure 4a–d**), indicating a redistribution of electron density within the fcu cavities. The absence of peak shifts or new reflections suggests that the crystal lattices remain largely unchanged, confirming a physisorption mechanism devoid of phase transitions or impurity formation.

We employed Rietveld refinement of synchrotron PXRD data for both CO_2-loaded frameworks to elucidate the host–guest interactions that

drive the superior gas adsorption/separation performance. The high quality of these refinements is evidenced by low R-weighted pattern (R_{wp}) values and small differences between the experimental and fitting profiles.

The refined structures reveal that the enhanced CO_2 capture in Y-MOF is rooted in a unique, high-affinity adsorption site where CO_2 is stabilised via a synergistic effect between the Lewis acidic Y^{3+} centres and the sequestered DMA-H^+ cations (**Figure 4e**). In this 'pincer-like' coordination, the cations act as intra-pore segmenting agents, effectively dividing the void into smaller, chemically active pockets[30]. Specifically, the N–H protons of DMA-H^+ and its localised positive charge density create a highly polarised environment that complements the electron-accepting nature of the yttrium nodes. This results in a multidentate interaction network that 'anchors' the CO_2 molecule through key short-range contacts: an $N_{DMA}\cdots O_{CO2}$ distance of 2.37 Å and a $Y\cdots O_{CO2}$ distance of 2.73 Å. These distances are consistent with a combination of synergistic hydrogen bonding and strong electrostatic interactions from the polarised Y^{3+} centres, where the metal centre functions as a Lewis acid to attract one oxygen atom of the CO_2 guest, while the positive charge of the DMA-H^+ cation stabilises the other.

Conversely, the neutral Zr-MOF framework lacks these stabilizing counteractions, resulting in significantly longer guest-to-framework distances (~3.63 Å) and weaker non-specific interactions (**Figure 4f**). In this environment, metal centres are heavily shielded by carboxylate oxygens, pushing the guest molecules toward the centre of the pore in a more disordered and mobile state. Consequently, adsorption in Zr-MOF is dominated by relatively weak, non-specific van der Waals interactions[31]. These atomic-scale insights reveal the interplay between the framework charge and the sequestered cations, which enhances the superior thermodynamic affinity of the Y-based framework.

These structural insights provide a molecular-level basis for the observed macroscopic behaviour. The localised 'electrostatic locking' in Y-MOF effectively constrains the rotational and translational degrees of freedom of the CO_2 molecules. This is consistent with its higher CO_2 uptake (85.11 $cm^3\ g^{-1}$), which is 46.4% greater than that of Zr-MOF (58.12 $cm^3\ g^{-1}$). This structural stabilisation directly results in a substantially elevated Q_{st} (38 vs. 28 kJ mol^{-1}) and enhanced selectivity over non-polar N_2 gas (10.59 vs. 9.46) compared to the neutral analogue. While the smaller effective pore diameter (4.1 Å and high-affinity sites in Y-MOF introduce greater diffusional resistance than the larger, vacant pores of Zr-MOF, the resulting separation purity window is significantly broader[32,33]. This confirms that counteraction-induced pore engineering is a critical determinant for achieving the high thermodynamic selectivity required for industrial fixed-bed operations.

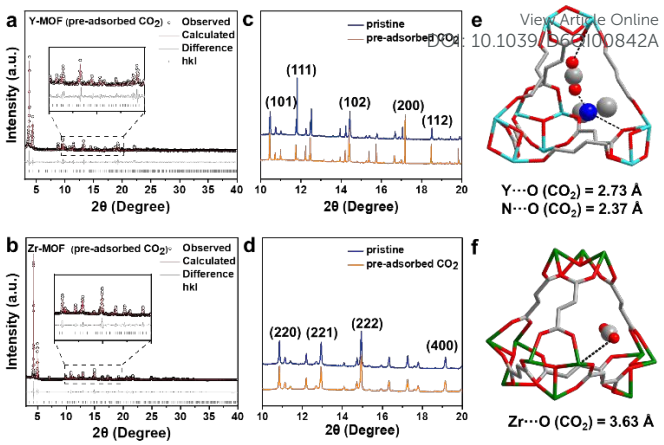

Figure 4. Rietveld refinement profiles for (**a**) Y-MOF and (**b**) Zr-MOF under CO_2 loading. Detailed comparison of synchrotron PXRD patterns before and after CO_2 adsorption of (**c**) Y-MOF and (**d**) Zr-MOF. Primary CO_2 binding sites for (**e**) Y-MOF and (**f**) Zr-MOF from Rietveld refinement. Ball-and-stick representation: light blue, Y; green, Zr; red, O; dark blue, N; grey, C. All structures were obtained by Rietveld refinement of high-resolution synchrotron PXRD (E = 20 keV) collected at 298 K. Detailed atomic parameters and crystallographic data are provided in **Table S6–S9**.

Conclusions

In conclusion, we have demonstrated, through a systematic comparative study of two isostructural fcu-type MOFs, that the introduction of extra-framework counteractions is a pivotal determinant of CO_2 capture performance. By transitioning from the neutral Zr-based framework to the anionic Y-based analogue, DMA-H^+ cations are strategically incorporated within the pore channels, fundamentally altering the adsorption environment. Although Zr-MOF possesses a higher specific surface area, its neutral pores lack the specific localised interactions required for high-affinity guest binding. In contrast, the presence of DMA-H^+ cations and Y^{3+} centres in Y-MOF synergistically creates a unique 'pincer-like' coordination environment. As confirmed by Rietveld refinement of synchrotron PXRD, this configuration generates localised electrostatic fields and synergistic hydrogen-bonding sites (N–H···O) that effectively lock CO_2 molecules in place. These molecular-level insights explain the 46.4% enhancement in CO_2 uptake and the significantly improved CO_2/N_2 selectivity observed in Y-MOF. Beyond these immediate performance metrics, the structural integrity and reversibility demonstrated over multiple cycles underscore the practical viability of this material. Ultimately, this strategy of cation-mediated pore engineering provides a versatile template for enhancing gas discrimination in other anionic framework topologies.

Conflicts of interest

There are no conflicts to declare.

Author contributions

View Article Online
DOI: 10.1039/D6QI00424A

Jing Ling conducted the main sample synthesis, experiments and data analysis; Zhiyu Tao assisted with TPD-MS testing; Jiafeng Miao assisted with breakthrough testing; Cong Lin, Hao Wang and Tsz Woon Benedict Lo designed the project and participated in the discussion and composition of the paper.

Data availability

The data supporting this article have been included as part of the Supplementary Information.

Acknowledgements

The authors thank the National Natural Science Foundation of China (22522207 and 22403080), Hong Kong Research Grants Council (C5081-21E and C5057-24E) and PolyU (P0058154 and P0047841) for financial support. The authors thank the synchrotron radiation facilities, SPring-8 (2023B1665, 2023B1666) and National Synchrotron Radiation Research Center (NSRRC; 2025-1-203-1), for the support on synchrotron PXRD and in-situ measurements. We also thank Research Centre for Carbon-Strategic Catalysis (RC-CSC), the University Research Facility in Materials Characterization and Device Fabrication (UMF) and the University Research Facility in Chemical and Environmental Analysis (UCEA) of PolyU for the support in material characterization.

References

1 S. Xiang, Y. He, Z. Zhang, H. Wu, W. Zhou, R. Krishna and B. Chen, Microporous metal-organic framework with potential for carbon dioxide capture at ambient conditions, *Nat. Commun.*, **2012**, *3*, 954.

2 S. Rekker, G. Chen, R. Heede, M. C. Ives, B. Wade and C. Greig, Evaluating fossil fuel companies' alignment with 1.5 °C climate pathways, *Nat. Clim. Change*, **2023**, *13*, 927–934.

3 J. A. Mason, T. M. McDonald, T.-H. Bae, J. E. Bachman, K. Sumida, J. J. Dutton, J. S. Kaye and J. R. Long, Application of a High-Throughput Analyzer in Evaluating Solid Adsorbents for Post-Combustion Carbon Capture via Multicomponent Adsorption of CO2, N2, and H2O, *J. Am. Chem. Soc.*, **2015**, *137*, 4787–4803.

4 E. S. Sanz-Pérez, C. R. Murdock, S. A. Didas and C. W. Jones, Direct Capture of CO2 from Ambient Air, *Chem. Rev.*, **2016**, *116*, 11840–11876.

5 R. L. Siegelman, E. J. Kim and J. R. Long, Porous materials for carbon dioxide separations, *Nat. Mater.*, **2021**, *20*, 1060–1072.

6 J.-B. Lin, T. T. T. Nguyen, R. Vaidhyanathan, J. Burner, J. M. Taylor, H. Durekova, F. Akhtar, R. K. Mah, O. Ghaffari-Nik, S. Marx, N. Fylstra, S. S. Iremonger, K. W. Dawson, P. Sarkar, P. H. J. Mercier, R. Singh, Q. Mao, Z. Baig and G. K. H. Shimizu, A scalable metal-organic framework as a durable physisorbent for carbon dioxide capture, *Science*, **2021**, *374*, 1464–1469.

7 L. Yu, S. Ullah, K. Zhou, Q. Xia, H. Wang, S. Tu, Y. Li, P. Li, S. Deng, Z. Li and J. Li, A Microporous Metal–Organic Framework Incorporating Both Primary and Secondary Building Units for Splitting Alkane Isomers, *J. Am. Chem. Soc.*, **2022**, *144*, 3766–3770.

8 H. Furukawa, F. Gándara, Y. B. Zhang, J. Jiang, W. L. Queen, M. R. Hudson, K. Njau, M. T. Kong, J. Rogers, A. S. Miller and O. M. Yaghi, Water adsorption in porous metal-organic frameworks and related materials, *J. Am. Chem. Soc.*, **2014**, *136*, 4369–4381.

9 A. H. Assen, T. Virdis, W. De Moor, A. Moussa, M. Eddaoudi, G. Baron and J. F. M. Denayer, Kinetic separation of C4 olefins using Y-fum-fcu-MOF with ultra-fine-tuned aperture size, *Chem. Eng. J.*, **2021**, *413*, 127388.

10 H. Wang, X. Dong, V. Colombo, Q. Wang, Y. Liu, W. Liu, X. L. Wang, X. Y. Huang, V. G. Proserpio, A. Sironi, Y. Han and J. Li, Tailor-Made Microporous Metal-Organic Frameworks for the Full Separation of Propane from Propylene Through Selective Size Exclusion, *Adv. Mater.*, **2018**, *30*, 1805088.

11 J. Bae, J. S. Choi, S. Hwang, W. S. Yun, D. Song, J. Lee, J. H. Kwak, H. C. Ham and D. H. Kim, Multiple Coordination Exchanges for Room-Temperature Activation of Open-Metal Sites in Metal–Organic Frameworks, *ACS Appl. Mater. Interfaces*, **2017**, *9*, 24743–24752.

12 B. T. W. Lo, L. Ye and S. C. E. Tsang, The Contribution of Synchrotron X-Ray Powder Diffraction to Modern Zeolite Applications: A Mini-review and Prospects, *Chem*, **2018**, *4*, 1778–1808.

13 B. T. W. Lo, L. Ye, J. Qu, J. Sun, J. Zheng, D. Kong, C. A. Murray, C. C. Tang and S. C. E. Tsang, Elucidation of Adsorbate Structures and Interactions on Brønsted Acid Sites in H-ZSM-5 by Synchrotron X-ray Powder Diffraction, *Angew. Chem. Int. Ed.*, **2016**, *55*, 5981–5984.

14 E. Arunan, G. R. Desiraju, R. A. Klein, J. Sadlej, S. Scheiner, I. Alkorta, D. C. Clary, R. H. Crabtree, J. J. Dannenberg, P. Hobza, H. G. Kjaergaard, A. C. Legon, B. Mennucci and D. J. Nesbitt, Definition of the hydrogen bond (IUPAC Recommendations 2011), *Pure Appl. Chem.*, **2011**, *83*, 1637–1641.

15 Y.-R. Miao, Z. Su and K. S. Suslick, Energy Storage during Compression of Metal–Organic Frameworks, *J. Am. Chem. Soc.*, **2017**, *139*, 4667–4670.

16 E. Quartapelle Procopio, F. Linares, C. Montoro, V. Colombo, A. Maspero, E. Barea and J. A. R. Navarro, Cation-exchange porosity tuning in anionic metal-organic frameworks for the selective separation of gases and vapors and for catalysis, *Angew. Chem. Int. Ed.*, **2010**, *49*, 7308–7311.

17 H. Wang, J. Zou and J. Li, Metal-organic frameworks with ftw-type connectivity: design, pore structure engineering, and potential applications, *CrystEngComm*, **2022**, *24*, 2189–2200.

18 W. Huang, K.-X. Li, Y. He, H. Yuan, P. Li, S. Chen and J. Li, Cation-exchanged MZSM-5 for CO2 adsorption: interplay of interaction potential and adsorption configuration, *Sep. Purif. Technol.*, **2026**, *386*, 136604.

19 Nugent, P., Belmabkhout, Y., Burd, S. *et al.* Porous materials with optimal adsorption thermodynamics and kinetics for CO_2 separation. *Nature*, ***2013***, 495, 80–84.

20 P. Kolodzeiski, I. de Vries, M. Strobl, L. Frentzel-Beyme, M. Paulus, C. Sternemann, H. J. Butler, K. S. Suslick and S. Henke, Understanding the High-Pressure Behavior of Honeycomb-Like Metal-Organic Frameworks with Open Metal Sites: Influence of Metal Identity, Linker Extension and Diamine Functionalization, *J. Am. Chem. Soc.*, **2025**, *147*, 46075–46084.

21 S. Yang, J. Sun, A. J. Ramirez-Cuesta, S. K. Callear, W. I. F. David, D. P. Anderson, R. Newby, A. J. Blake, J. E. Parker, C. C. Tang and M. Schröder, Selectivity and direct visualization of carbon dioxide and sulfur dioxide in a decorated porous host, *Nat. Chem.*, **2012**, *4*, 887–894.

22 P. M. Bhatt, Y. Belmabkhout, A. H. Assen, Ł. J. Weseliński, H. Jiang, A. Cadiau, D. X. Xue and M. Eddaoudi, Isoreticular rare earth fcu-MOFs for the selective removal of H2S from CO2 containing gases, *Chem. Eng. J.*, **2017**, *324*, 392–396.

23 Z. Chen, M. A. Mian, S. J. Lee, H. Chen, X. Zhang, K. A. Kirlikovali, S. Shafaie, S. Alayoglu, J. J. Snider, T. Islamoglu and J. R. Long, Fine-Tuning a Robust Metal-Organic Framework

View Article Online
DOI: 10.1039/D6QI00842A

toward Enhanced Clean Energy Gas Storage, *J. Am. Chem. Soc.*, **2021**, *143*, 18838–18843.
24 J.-R. Li, J. Sculley and H.-C. Zhou, Metal–Organic Frameworks for Separations, *Chem. Rev.*, **2012**, *112*, 869–932.
25 J. D. Humby, O. Benson, G. L. Smith, S. P. Argent, I. da Silva, Y. Cheng, W. I. F. David, S. Yang and M. Schröder, Host–guest selectivity in a series of isoreticular metal–organic frameworks: observation of acetylene-to-alkyne and carbon dioxide-to-amide interactions, *Chem. Sci.*, **2019**, *10*, 1098–1106.
26 J. M. Kolle, M. Fayaz and A. Sayari, Understanding the Effect of Water on CO2 Adsorption, *Chem. Rev.*, **2021**, *121*, 7280–7345.
27 Y. P. Chen, Y. Liu, D. Liu, M. Bosch and H.-C. Zhou, Direct measurement of adsorbed gas redistribution in metal-organic frameworks, *J. Am. Chem. Soc.*, **2015**, *137*, 2919–2930.
28 Y. Chen, W. Lu, M. Schröder and S. Yang, Analysis and Refinement of Host–Guest Interactions in Metal–Organic Frameworks, *Acc. Chem. Res.*, **2023**, *56*, 2569–2581.
29 H. Wu, W. Zhou and T. Yildirim, High-capacity methane storage in metal-organic frameworks M2(dhtp): the important role of open metal sites, *J. Am. Chem. Soc.*, **2009**, *131*, 4995–5000.
30 S. Dai, X. Zeng, B. J. Moore, Y. Zhu, Y. Yang, Z. Wang and S. J. Rowan, Light-Induced Binding and Reduction of CO2 over Transient Open Ce(III) Sites in a Metal–Organic Framework, *J. Am. Chem. Soc.*, **2026**, *148*, 11749–11757.
31 S.-C. Fan, Y.-P. Li, J.-W. Wang, X. C. Xing, Z. Y. Liu, W. Yuan and J. R. Li, Local-Global Synergistic Pore Space Partition in Metal–Organic Frameworks for Boosting CO2 Capture and Conversion, *J. Am. Chem. Soc.*, **2025**, *147*, 39379–39390.
32 J. H. Carter, X. Han, F. Y. Moreau, I. da Silva, A. Nevin, H. G. W. Godfrey, S. Yang and M. Schröder, Exceptional Adsorption and Binding of Sulfur Dioxide in a Robust Zirconium-Based Metal–Organic Framework, *J. Am. Chem. Soc.*, **2018**, *140*, 15564–15567.
33 L. Guo, X. Han, Y. Ma, J. Li, W. Lu, W. Li, S. Yang and M. Schröder, High capacity ammonia adsorption in a robust metal–organic framework mediated by reversible host–guest interactions, *Chem. Commun.*, **2022**, *58*, 5753–5756.

View Article Online
DOI: 10.1039/D6QI00842A

The data supporting this article have been included as part of the Supplementary Information.